

Origins of chalcogenide perovskite instability

Adelina Carr^a, Talia Glinberg^b, Nathan Stull^c, James R. Neilson^{c,d}, Christopher J. Bartel^{a*}

^a University of Minnesota, Department of Chemical Engineering and Materials Science, Minneapolis, MN 55455

^b University of Minnesota, Department of Chemistry, Minneapolis, MN 55455

^c Colorado State University, Department of Chemistry, Fort Collins, CO 80523

^d Colorado State University, School of Materials Science & Engineering, Fort Collins, CO 80523

* correspondence to cbartel@umn.edu

Abstract

Chalcogenide perovskites, particularly II-IV $AB\text{S}_3$ compounds, are a promising class of materials for optoelectronic applications. However, these materials frequently exhibit instability in two respects: 1) a preference for structures containing one-dimensional edge- or face-sharing octahedral networks instead of the three-dimensional corner-sharing perovskite framework (polymorphic instability), and (2) a tendency to decompose into competing compositions (hull instability). We evaluate the stability of 81 $AB\text{S}_3$ compounds using Density Functional Theory, finding that only BaZrS_3 and BaHfS_3 are both polymorphically and hull stable, with the NH_4CdCl_3 -type structure the preferred polymorph for 77% of these compounds. Comparison with existing tolerance factor models demonstrates that these approaches work well for known perovskites but overpredict stability for compositions without published experimental results. Polymorphic stability analysis reveals that perovskite structures are stabilized by strong B - S bonding interactions, while needle structures exhibit minimal B - S covalency, suggesting that electrostatic rather than covalent interactions drive the preference for edge-sharing motifs. Hull stability analysis comparing $AB\text{S}_3$ to $AB\text{O}_3$ analogues reveals a weaker inductive effect in sulfides as a possible explanation for the scarcity of sulfides compared with oxides. The relative instability of $AB\text{S}_3$ compounds is further supported by experimental synthesis attempts. These findings provide fundamental insights into the origins of instability in chalcogenide perovskites and highlight the challenges in expanding this promising materials class beyond the few materials that have been reported to date.

Introduction

Chalcogenide perovskites have garnered significant attention for optoelectronic applications.¹ These materials exhibit smaller bandgaps than oxides,² greater thermal and chemical stability than hybrid organic-inorganic halides,^{3,4} and additional features like high absorption coefficients and defect-tolerant carrier transport that enhance their functionality.^{5,6}

This class of materials follows the general formula ABX_3 , where A and B are cations and X is a chalcogenide anion (S, Se, Te). This work focuses on the most well-studied subset of these materials where A is divalent, B is tetravalent, and X is sulfur, excluding compounds that are radioactive or contain f -electrons due to their limited relevance for optoelectronic applications. While the ideal perovskite structure is cubic, chalcogenide perovskites rarely adopt this high-symmetry structure.⁷ Instead, they typically crystallize in distorted perovskite polymorphs due to the larger, more polarizable chalcogenide anions and non-ideal cation-anion radii ratios. Among these, the $GdFeO_3$ -type orthorhombic perovskite is the most commonly observed.¹ As shown in **Figure 1a**, this structure consists of a three-dimensional network of tilted corner-sharing BS_6 octahedra, with the larger A -site cations occupying the interstitial voids. This 3D network plays a crucial role in enabling high and isotropic carrier mobility, direct bandgaps, and other optoelectronic properties.⁸ While most research into ABS_3 materials focuses on the perovskite structure, these compounds often exhibit a tendency to form alternative structures featuring face- or edge-sharing octahedra, which can lead to different electronic and structural properties.^{1,9–11}

The three most common polymorphs of ABS_3 chalcogenides (including orthorhombic perovskite) are depicted in **Figure 1**. The $BaNiO_3$ -type hexagonal structure (**Figure 1b**) consists of a one-dimensional network of face-sharing octahedra, while the NH_4CdCl_3 -type “needle-like” structure (**Figure 1c**) is characterized by a one-dimensional framework of edge-sharing octahedra. These three polymorphs are the focus of this study, but it is worth noting that other structures have been experimentally observed, such as “misfit layered structures” and variants containing mixed edge- and face-sharing octahedra.^{12–16}

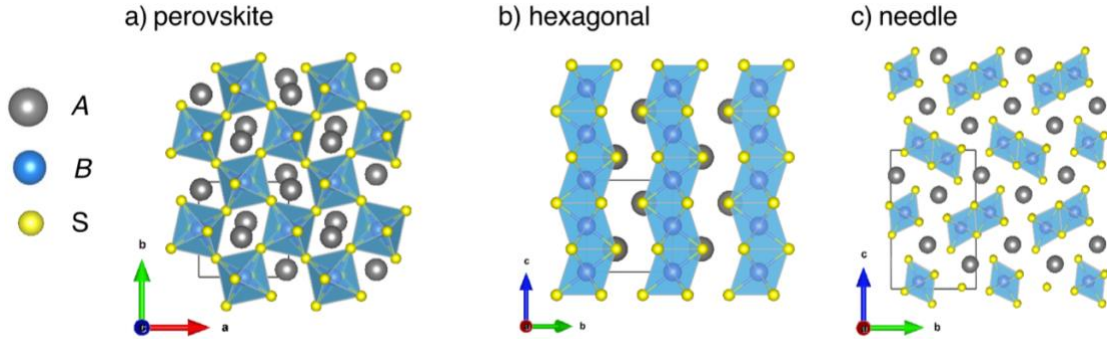


Figure 1. Common polymorphs of ABS_3 compounds. a) $GdFeO_3$ -type orthorhombic perovskite, b) $BaNiO_3$ -type hexagonal and c) NH_4CdCl_3 -type “needle-like” structure. Gray spheres represent A -site cations, blue spheres represent B -site cations, and yellow spheres represent sulfur.

Although numerous ABS_3 compounds within our scope have been synthesized in various structures, only the six compounds spanning $A = Ba, Sr, Ca$ and $B = Zr, Hf$ have been synthesized in the perovskite structure.¹ $SrZrS_3$ is unique among this group in that it has been synthesized in both the perovskite and needle structures, with perovskite emerging as the higher temperature phase.^{17,18} $BaZrS_3$ is the most well studied for its promising

optoelectronic properties and has been synthesized at a number of conditions, including low-temperatures colloidal synthesis.^{5,19–22} However, the most common synthetic approach to realize these materials is high-temperature sulfurization of their oxide perovskite analogues,¹⁹ with CaHfS_3 and CaZrS_3 requiring comparatively higher temperatures than the $A = \text{Ba}, \text{Sr}$ counterparts.^{21,23}

Previous computational studies have evaluated the thermodynamic stability of various subsets of chalcogenide perovskites.^{12,24–28} For example, Huo, *et al.* used Density Functional Theory (DFT) with the PBE functional²⁹ to study 168 ABX_3 compounds (Including $X = \text{S}, \text{O}, \text{Se}$) in four different crystal structures: cubic perovskite, orthorhombic perovskite, hexagonal, and needle. They found that $\sim 30\%$ adopted a perovskite ground state, including sulfides with $A = \text{Ba}, \text{Ca}$ and $B = \text{Hf}, \text{Zr}$.²⁷ Brehm *et al.* used LDA³⁰ to study ABS_3 compounds with d^0 configurations¹² (including I-V and II-IV valences for $A-B$) and found none had a perovskite ground state; instead, BaZrS_3 was calculated in that study to prefer the needle structure. Their finite-temperature analysis, however, showed that perovskites are stabilized at elevated temperatures for systems with $A = \text{Ba}, \text{Sr}, \text{Sn}, \text{or Pb}$ and $B = \text{Zr}$. In addition to polymorphic stability, some studies have also considered the stability of ABX_3 compounds against decomposition into competing phases.^{24,25} For example, Körbel *et al.* computed ternary phase diagrams for a broad range of ABX_3 compounds (not limited to chalcogenides), identifying BaHfS_3 , BaZrS_3 , and BaZrSe_3 as the only chalcogenide perovskites within 25 meV/atom of stability according to their calculated convex hull.²⁴

In parallel to thermodynamic analyses with DFT, tolerance factor models have long been used to assess the tendency for ABX_3 materials to crystallize in perovskite or non-perovskite structures (in this work, perovskite refers to materials comprised of corner-sharing BS_6 octahedra surrounding an A -site cation). The most well-known of these models is the Goldschmidt tolerance factor,³¹ which relies only on geometric considerations and the ionic radii of constituent elements, usually Shannon's ionic radii calibrated for oxides.³² While this model and subsequent refinements³³ have worked well for oxide and halide perovskites, its accuracy declines when applied to non-oxide chalcogenides.^{1,34,35}

Recent efforts have sought to improve tolerance factor models for chalcogenide perovskites. In 2022, Jess *et al.* introduced a modified tolerance factor, recognizing that the significantly lower electronegativity of sulfur compared to oxygen results in greater covalent bonding.³⁴ To account for this, their model introduced an electronegativity-weighted correction to the Goldschmidt tolerance factor:

$$t^* = \frac{\frac{\Delta\chi_{(A-X)}}{\Delta\chi_{(A-O)}}(r_A + r_X)}{\sqrt{2} \frac{\Delta\chi_{(B-X)}}{\Delta\chi_{(B-O)}}(r_B + r_X)} \quad (1)$$

Where $\Delta\chi$ represents the electronegativity differences between the indicated sites, and r_A , r_B and r_X are the ionic radii for the A , B , and X sites, respectively. This electronegativity-modified tolerance factor successfully grouped 9 experimentally known chalcogenide perovskites within $0.94 < t^* < 1.12$ (BaZrS₃, BaHfS₃, SrZrS₃, SrHfS₃, CaZrS₃, CaHfS₃, EuZrS₃, EuHfS₃, and BaUS₃) with no known non-perovskites falling within this interval.

In 2024, Turnley *et al.* introduced another tolerance factor based approach,³⁵ noting a key limitation in previous models: the ionic radii data used in traditional tolerance factors (Shannon's dataset) was empirically derived from metal oxides and fluorides, assuming ionic bonding. However, the lower electronegativity of sulfides yields a tendency for stronger covalent interactions, making the oxide-calibrated radii less applicable to chalcogenide perovskites. Shannon recognized this issue and created a separate dataset of metal-sulfide-derived radii, although this dataset remains less extensive.³⁶ Turnley *et al.* used this sulfide-derived radii dataset (extrapolated where necessary) to establish a refined perovskite stability criterion. Their screening method involves three metrics. First, materials were screened using the octahedral factor ($\mu = r_B/r_X$) to determine whether B and X -site ions were appropriately sized to form stable octahedra. Materials passing the octahedral factor test ($0.414 < \mu < 0.732$) were then evaluated based on a modified Goldschmidt tolerance factor using sulfide-derived radii (t^S), constrained within $0.865 \leq t^S \leq 0.965$ along with an electronegativity-based metric, $\chi_{\text{diff}} = 1/5 (3\chi_S - \chi_A - \chi_B)$, requiring $\chi_{\text{diff}} \geq 1.025$ for perovskite stability. In their study, Turnley *et al.* applied this multi-step screening method to 100 compounds from the Materials Project database of DFT calculations,³⁷ 24 of which are experimentally known chalcogenide perovskites. Among those, their tolerance factor model correctly identified 18 as lying within the proposed stability window, including f -electron and radioactive elements, as well as materials belonging to different valence families (e.g., III–III compounds). When restricting the comparison to the six experimentally reported chalcogenide perovskites within our scope, the Turnley model successfully places all six within the predicted perovskite stability window.

While tolerance factors are a valuable tool for assessing perovskite stability, they intrinsically focus only on polymorphic stability and do not probe the tendency for decomposition into competing compositions (hull stability).³⁸ Both polymorphic and hull stability can be evaluated using DFT calculations but through different approaches. Polymorphic stability is determined by comparing total energies at 0 K across different polymorphs, with the lowest-energy structure defined as the ground state. The energy difference between a given polymorph and the ground state is denoted as ΔE_{gs} . Hull stability, assessed via the convex hull formalism, requires computing formation energies for all ground-state structures in a given chemical space (e.g., AS , BS_2 , etc., for A - B - S in ABS_3). A material is considered hull-stable if its formation energy is negative and lower than any linear combination of competing phases in that chemical space. The decomposition energy (ΔE_d) quantifies the energy difference relative to the most stable phase-separated state, with

stability requiring $\Delta E_d \leq 0$. Materials with $\Delta E_d > 0$ are computed to be unstable with respect to decomposition but may still be synthetically accessible metastable phases if ΔE_d and ΔE_{gs} are not too large.³⁹

In this study, we used DFT calculations at the meta-GGA level of theory⁴⁰ to assess the polymorphic and hull stability of 81 ABS_3 chalcogenides and probed the two recently introduced tolerance factors in the context of our DFT-calculated thermodynamics. Our study highlights the sparsity of thermodynamically stable chalcogenide perovskites and proposes thermodynamic and chemical origins for their instability.

Methods

Computational Details. All DFT calculations were performed using the Vienna Ab Initio Simulation Package^{41,42} (VASP, version 6.4.1) and the projector augmented wave (PAW) method.^{43,44} A plane-wave energy cutoff of 520 eV, and Γ -centered k-point grid with a minimum spacing between k-points of 0.22 \AA^{-1} (KSPACING in VASP), were used for all calculations. To assess the thermodynamic stability of various ABS_3 compounds, the r²SCAN meta-generalized gradient approximation (meta-GGA) density functional was applied.⁴⁰ The convergence criteria were set as 10^{-6} eV for electronic optimization and $0.03 \text{ eV} \cdot \text{\AA}^{-1}$ for ionic relaxation.

The initial structures for the 81 ABS_3 compounds investigated in this study were generated by applying atomic substitutions to three prototype structures queried from the Materials Project database³⁷: GdFeO_3 (orthorhombic perovskite), BaNiO_3 (hexagonal), and SrZrS_3 (needle-like), which are representative of stable polymorphs in their respective structure types. After substitution, all structures were optimized using the calculation settings mentioned above. Polymorphic stability was assessed by comparing DFT total energies at 0 K across the three polymorphs for each composition. Hull stability was evaluated by querying all competing phases in each A - B - S phase diagram from the Materials Project database³⁷ and recomputing all formation energies using the aforementioned calculation settings.

The LOBSTER package⁴⁵ was used for COHP⁴⁶ analysis. Charge analysis was performed via the Bader method.^{47,48} Structures and charge densities were analyzed using VESTA⁴⁹. Pymatgen was used to prepare and analyze DFT and LOBSTER calculations.^{50,51}

For tolerance factor analysis, ionic radii were taken directly from the supplementary data of the respective studies (Jess *et al.*, Turnley *et al.*) and used as reported.^{34,35}

Experimental details. Reactions targeting the synthesis of CaTiS_3 and BaZrS_3 were carried out by the attempted boron-assisted sulfidation of the corresponding oxide perovskites, CaTiO_3 and BaZrO_3 .^{52,53} All manipulations were performed in air unless explicitly specified. The oxide precursors were prepared by mixing stoichiometric amounts

of the alkaline earth carbonates, CaCO_3 (Sigma-Aldrich 99%) BaCO_3 (J.T. baker 99%), with the corresponding transition metal oxides, ZrO_2 (Sigma-Aldrich 99%) and TiO_2 (Aldrich Chemical 99.9%), in an agate mortar with a small amount of isopropanol for 15 min and evaporated to dryness. The powders were then pelletized in a 0.5 in die to 2 tons of force, placed in an alumina crucible and heated in a tube furnace to 1100 °C at a ramp rate of 10 °C/min and held at temperature in air for 24 h. For the sulfidation reaction, stoichiometric amounts of oxide perovskite precursor and sulfur (NOAH Technology Corporation 99.5%), with an excess 2.2 molar ratio of boron (Aldrich Chemistry 95%) targeting $\text{AMO}_3 + 2.2 \text{ B} + 3 \text{ S}$, were ground in an agate mortar for 15 min and loosely packed within an alumina crucible that was held in an extruded quartz ampule. These ampules (16 mm O.D.; 14 mm I.D.) were flame sealed under vacuum (~ 15 mTorr) and placed into a muffle furnace. The reaction with CaTiO_3 initially showed significant reaction with the SiO_2 ampule. As such, the reaction was repeated in a stainless-steel tube, 3/8" inner diameter (no Al_2O_3 crucible). The tube was crimped closed and then welded using an MRF Arc Melt Furnace under ~ 0.85 atm of argon. All samples were then heated at a ramp rate of 5 °C/min to 300 °C and 600 °C with holding times of 5 h each, then finally to 1000 °C for a holding time of 36 h. The samples were let to furnace cool and opened in air for analysis.

Powder X-ray diffraction (PXRD) measurements were conducted using a Cu $\text{K}\alpha$ X-ray source and a LynxEye XE-T position-sensitive detector on a Bruker D8 Discover diffractometer to verify phase purity. Before measurement, the samples were placed on a "zero diffraction" Si wafer, immobilized with petroleum jelly. Quantitative phase analysis employing the Rietveld method was performed using TOPAS v6.

Results and discussion

To better understand previous experimental and computational results, we considered a subset of the materials evaluated in the Jess *et al.*, work.³⁴ We selected 6 ABS_3 compounds predicted by this tolerance factor to be perovskite as well as 39 ABS_3 compounds that lie near the borders of perovskite stability with respect to this tolerance factor. An additional 36 ABS_3 compounds were computed to consider all A/B combinations spanned by these 45 compounds. For each of these 81 compounds, we performed DFT calculations in the distorted perovskite, needle, and hexagonal polymorphs using the r^2SCAN meta-GGA functional.⁴⁰ In **Figure 2**, we show the DFT-predicted thermodynamic stability of the analyzed compounds. These stabilities were assessed in two ways: ΔE_{gs} indicates the difference in energy between the perovskite structure and the corresponding ground-state polymorph; ΔE_{d} indicates the decomposition energy for the ground-state polymorph and is calculated by considering all competing phases available in the Materials Project database³⁷ (recomputed with r^2SCAN in this work). All ΔE_{gs} , ΔE_{d} and calculated ground state structures are listed in **Table S1**. An ABS_3 compound is thermodynamically stable in the perovskite structure if ΔE_{gs} and ΔE_{d} are both ≤ 0 . The magnitude of thermodynamic instability for a perovskite-structured ABS_3 is then given by the sum of ΔE_{gs} and ΔE_{d} . Compounds that have been previously synthesized

in any polymorph are highlighted in blue, and the shape of the marker indicates the DFT-calculated ground-state structure.

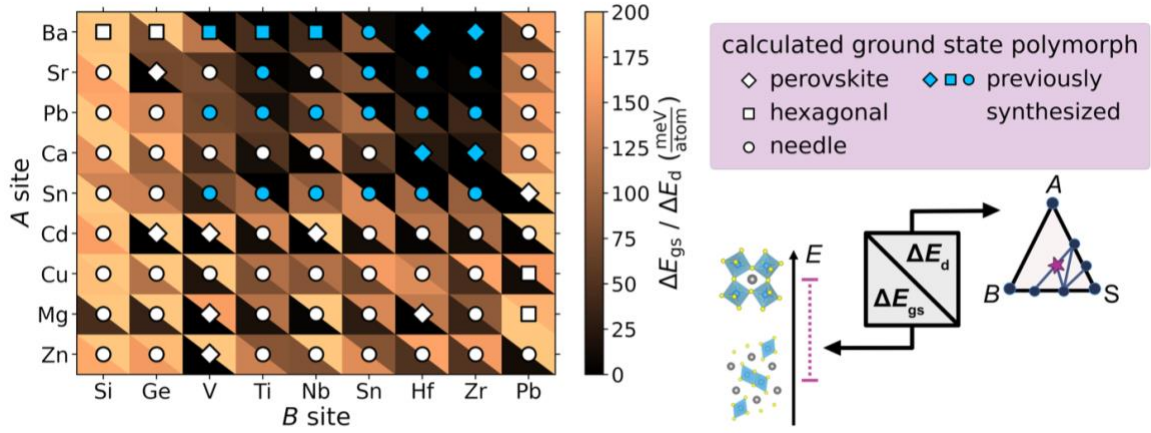


Figure 2. Heatmap summarizing the thermodynamic stability of 81 selected ABS_3 compounds. Each square corresponds to a unique ABS_3 compound, with A -site elements on the y -axis and B -site elements on the x -axis. Each lower left triangle shows the polymorphic instability, ΔE_{gs} , for the perovskite structure (a value of 0 indicates that perovskite is the ground-state structure). Each upper right triangle indicates the decomposition energy, ΔE_d , relative to the A - B - S convex hull (a value of 0 indicates that the ground-state structure is thermodynamically stable with respect to decomposition into competing compounds). Marker shapes indicate the DFT-predicted ground-state polymorph, and blue-filled markers denote compounds that have been previously synthesized (in any structure).

Our calculations show that all 24 of the previously synthesized ABS_3 materials (in any polymorph) have $\Delta E_d < 90$ meV/atom with 20/24 having $\Delta E_d < 30$ meV/atom. We should note that in some cases, exotic synthetic approaches (such as high pressure) were used to access the materials (as is the case with $ASnS_3$, where $A = Ba, Pb, Sr$).^{14,54} Among the materials considered that have not yet been synthesized, 7 have $\Delta E_d \leq 90$ meV/atom, including three with $\Delta E_d < 61$ meV/atom ($CaTiS_3$, $CaSnS_3$ and $SrVS_3$). For context, a previous study analyzing over 29,000 materials in the Materials Project database found that 90% of synthesized metastable materials are within 67 meV/atom of the hull.³⁹ While these numbers provide a helpful reference for assessing metastability, it is important to emphasize that being below this threshold does not guarantee synthesizability. It is possible that there are no thermodynamic conditions under which a specific material is thermodynamically accessible, even if it has a weakly positive ΔE_d . These results highlight the sparsity of ABS_3 compounds that are thermodynamically stable or weakly unstable with respect to decomposition into competing phases in each A - B - S chemical space.

As for ΔE_{gs} , our calculations predict that 12 of 81 compounds have perovskite ground states ($\Delta E_{gs} = 0$). This includes 4 of the 6 compounds that have been previously synthesized in the perovskite structure ($BaHfS_3$, $BaZrS_3$, $CaHfS_3$ and $CaZrS_3$). The two remaining experimentally known perovskites within our scope are $SrZrS_3$ and $SrHfS_3$, which have

marginal polymorphic instability (ΔE_{gs} of 6 and 8 meV/atom, respectively). Importantly, many of these compounds with perovskite ground states exhibit hull instabilities (as discussed later). Of ABS_3 compounds that have been synthesized in non-perovskite polymorphs, the least unstable perovskite is SnVS_3 with $\Delta E_{\text{gs}} = 31$ meV/atom. As with ΔE_{d} , it is possible that ABS_3 compounds with $\Delta E_{\text{gs}} > 0$ could be synthesized in the perovskite structure. A previous study proposed using the energy of the amorphous phase as a physically meaningful upper bound for ΔE_{gs} ,⁵⁵ but this relatively generous upper bound varies widely from compound to compound. In the absence of exotic synthetic approaches, the probability of accessing a perovskite-structured ABS_3 should decrease substantially for compounds with larger ΔE_{gs} , and it is notable that the largest ΔE_{gs} of any previously reported perovskite is only 8 meV/atom (SrHfS_3).

Assessing polymorphic and hull stability together, ABS_3 compounds where perovskites could plausibly be synthesized are indicated by black or nearly black squares in **Figure 2**. Six of the 81 compounds we calculated have been previously synthesized in the perovskite structure (BaZrS_3 , BaHfS_3 , CaZrS_3 , CaHfS_3 , SrZrS_3 , SrHfS_3). BaZrS_3 and BaHfS_3 are the only compounds in our study calculated to be ground-state perovskites ($\Delta E_{\text{gs}} = 0$) and stable against competing phases ($\Delta E_{\text{d}} \leq 0$). CaZrS_3 and CaHfS_3 are also calculated to have perovskite ground states but are slightly above the convex hull ($\Delta E_{\text{d}} = 25$ and 27 meV/atom, respectively). SrZrS_3 and SrHfS_3 are calculated to have needle ground states that lie on the convex hull ($\Delta E_{\text{gs}} = 6$ and 8 meV/atom, respectively). Considering all 81 compounds in our study, two key observations emerge: (1) the needle structure is overwhelmingly preferred as the ground-state structure, accounting for 77% of the 81 materials analyzed, and (2) thermodynamically stable perovskites are sparse with only two of 81 compounds having $\Delta E_{\text{gs}} = 0$ and $\Delta E_{\text{d}} \leq 0$.

Given the limited number of stable perovskites and the challenges in synthesizing those calculated to be unstable, it is natural to ask whether tolerance factors can reliably predict perovskite formability in chalcogenides beyond the previously synthesized materials used to develop these models. In **Figure 3a**, we show a comparison between the Jess tolerance factor³⁴ (x -axis) and the DFT-calculated ΔE_{gs} (y -axis). The gray-shaded region marks the range where this tolerance factor predicts a stable perovskite ($0.92 < t^* < 1.10$). For clarity, this figure shows a zoomed-in view of the data with the full range available in **Figure S1**. This comparison shows that Jess tolerance factor predictions largely deviate from the DFT predictions for many hypothetical compounds. For example, SnGeS_3 strongly favors the needle structure ($\Delta E_{\text{gs}} = 131$ meV/atom) but is predicted to be a stable perovskite by the tolerance factor ($t^* = 0.99$).

A similar comparison is shown in **Figure 3b** for the Turnley tolerance factor,³⁵ highlighting only the 45 compounds we assessed that pass the octahedral factor filter ($0.414 < \mu < 0.732$). As was done in Ref. ³⁵, each of these compounds are shown with respect to the

sulfide-adjusted Goldschmidt tolerance factor t^S (x -axis) and the electronegativity difference, $\chi_{\text{diff}} = 1/5 (3\chi_S - \chi_A - \chi_B)$ (y -axis). Points are colored by their calculated ΔE_{gs} with lighter points being less stable in the perovskite structure. Turnley *et al.*, identified a perovskite stability window in the range $0.865 < t^S < 0.965$ and $\chi_{\text{diff}} > 1.025$ (shaded gray in **Figure 3b**). Five materials with DFT-predicted perovskite ground-states from our study fall within this window, along with four other compounds calculated to have non-perovskite ground states. There appears to be a relationship between electronegativity and energetic ordering, where compounds with a lower ΔE_{gs} tend to cluster at higher χ_{diff} values. There is no clear trend along the t^S axis, reinforcing that this modified Goldschmidt model also fails to capture a trend with energetic ordering. Calculated values for both tolerance factors and their predicted stable structures are provided in **Table S1**, along with the ionic radii, μ , and χ_{diff} values used in the calculations.

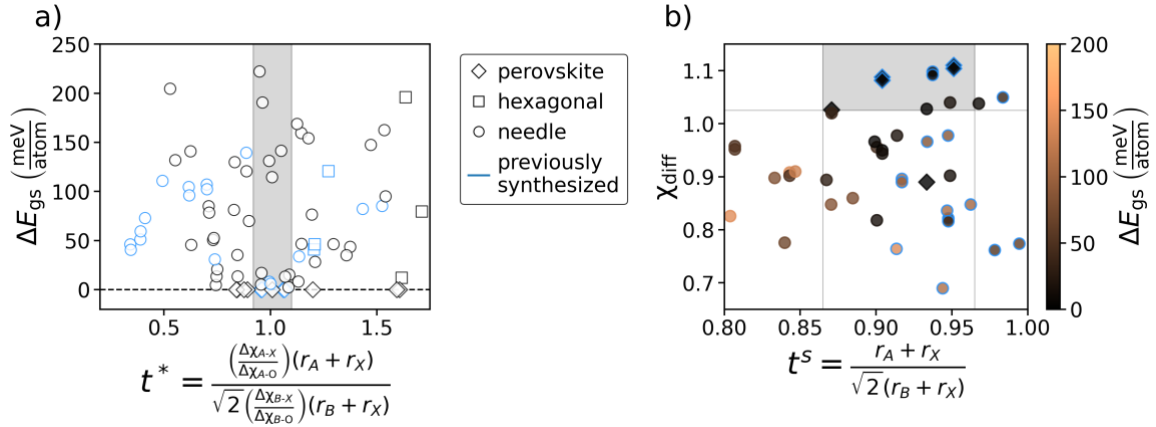


Figure 3. a) DFT-predicted energy difference between the perovskite structure and the corresponding ground-state structure (ΔE_{gs}) plotted against the Jesse tolerance factor (t^*), where points at $\Delta E_{\text{gs}} = 0$ indicate a perovskite ground state. The gray region denotes the t^* range where this tolerance factor predicts perovskite stability. b) The electronegativity difference, χ_{diff} , plotted against the Turnley tolerance (t^S). The color bar corresponds to the same DFT-calculated ΔE_{gs} . The gray region denotes the t^S range above a certain χ_{diff} where the Turnley tolerance factor predicts stable perovskites. In both plots, blue-outlined data points denote previously synthesized compounds (in any structure), and marker shapes indicate the DFT-predicted ground-state structure: diamonds for perovskite, circles for needle, and squares for hexagonal.

Together, these analyses highlight the need for a more comprehensive framework to accurately predict chalcogenide perovskite stability. In both cases, there is limited correlation between the tolerance factor and ΔE_{gs} as we would expect ΔE_{gs} to be minimal in the gray shaded region and increase as t^* or t^S deviates from the perovskite-stable region. Furthermore, while both models perform well for previously synthesized materials, their boundaries were empirically defined based on these previously synthesized perovskites. Our results suggest that even electronegativity-adjusted tolerance factors often overpredict chalcogenide perovskite stability, emphasizing that the interactions in these systems are more

nuanced than those captured by these models. Motivated by this, we aimed to uncover the factors that dictate polymorphic and hull (in)stability.

Analysis of polymorphic instabilities

To go beyond geometric considerations and better understand why chalcogenides favor non-perovskite motifs (e.g., edge-sharing octahedra), we turn to the role of covalency and chemical bonding—particularly how the lower electronegativity of sulfur compared to oxygen may contribute to destabilizing the corner-sharing network that is so common in oxides. Previous studies have shown that even in oxide perovskites, increased covalency leads to destabilization of the perovskite, which is further exacerbated by oxide ion polarization.⁵⁶ Here, integrated Crystal Orbital Hamilton Population (ICOHP)⁴⁶ was used as an analytical tool to observe trends in covalent interactions among $AB\text{S}_3$ polymorphs. We mainly compare the perovskite and needle structures due to the strong preference for the needle structure exhibited by the compounds studied in this work.

Analysis of our COHP results suggests that covalent interactions tend to preferentially stabilize the perovskite structure over the needle structure, which is surprising given the overwhelming stability of the needle structure. As shown in **Figure 4**, covalent $B\text{--}S$ interactions differ substantially between the two structure types. Compounds that adopt the perovskite ground state (and those with low ΔE_{gs}) typically exhibit strong $B\text{--}S$ covalency within their BS_6 octahedral units. In contrast, compounds that crystallize in the needle structure often show little to no $B\text{--}S$ covalency, and consistently less than their perovskite counterparts. Due to the relatively large atomic radius of sulfur (compared to oxygen), both structure types display considerable $S\text{--}S$ overlap. As shown in **Figure S2**, many compounds exhibit similar $S\text{--}S$ antibonding interactions near the Fermi level in both the perovskite and needle structures.

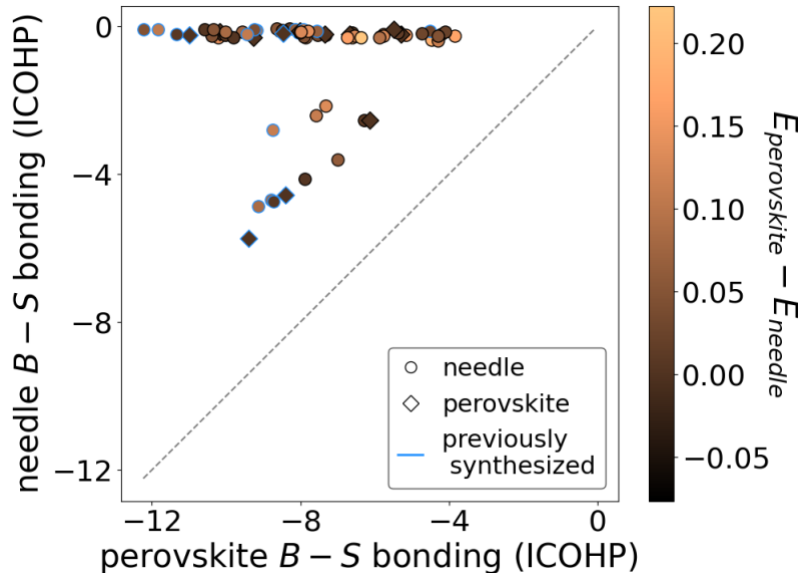


Figure 4. Parity plot comparing integrated COHP (ICOHP) values for B - S bonding interactions in the needle and perovskite structures, normalized per formula unit and integrated from 0 to -7 eV below the Fermi level. More negative values indicate more bonding interactions. Points are colored according to the difference in energy from the perovskite to the needle structures. Points outlined in blue correspond to previously synthesized materials. Diamond-shaped markers represent materials that have a perovskite ground state, while circles represent a needle ground state (according to our calculations). Because we compare needle and perovskite only, we have excluded materials with a hexagonal ground state. Here, we have only considered materials with differing A - and B -site atoms. The units for ICOHP are arbitrary.

To understand how these distinct covalency trends emerge in these two structure types, CaHfS_3 is presented in **Figure 5** as a representative example. In **Figure 5a** and **5c**, we compare the COHP of CaHfS_3 in the perovskite (a) and needle structures (c). Both structures exhibit similar S-S antibonding interactions near the Fermi level, arising from the relatively large electron cloud of the sulfide anion, overlapping within and between octahedra in each structure. In contrast, the Hf-S bonding in the perovskite structure is markedly stronger with a large peak in $-\text{COHP} > 0$ (bonding interactions), whereas the needle structure exhibits effectively no Hf-S covalency. In **Figure 5b** and **5d**, we compare the real space charge densities for this same energy interval in each structure. Within the chosen 2D slices of the charge density, the perovskite structure exhibits a linked network of tilted corner-sharing octahedra with substantial covalent Hf-S bonding. In contrast, the edge-sharing octahedra of the needle structure have very little charge density lying between Hf and S ions, instead favoring high density on each S ion.

This analysis reveals that the small number of perovskites that are lower in energy than their needle counterparts are stabilized by B - S covalent bonding interactions. Recalling that the needle structure is by far the most common ground state among ABS_3 compounds (77% of compounds analyzed in this work), our results rule out covalency as the origin of

this preference for the needle structure. It is instead plausible that the needle structure offers a more favorable electrostatic arrangement. This notion is supported by previous work from Young and Rondinelli on halide perovskites (e.g., CsPbI₃), where electrostatic interactions were found to be the primary origin of stability in the needle structure.⁵⁷

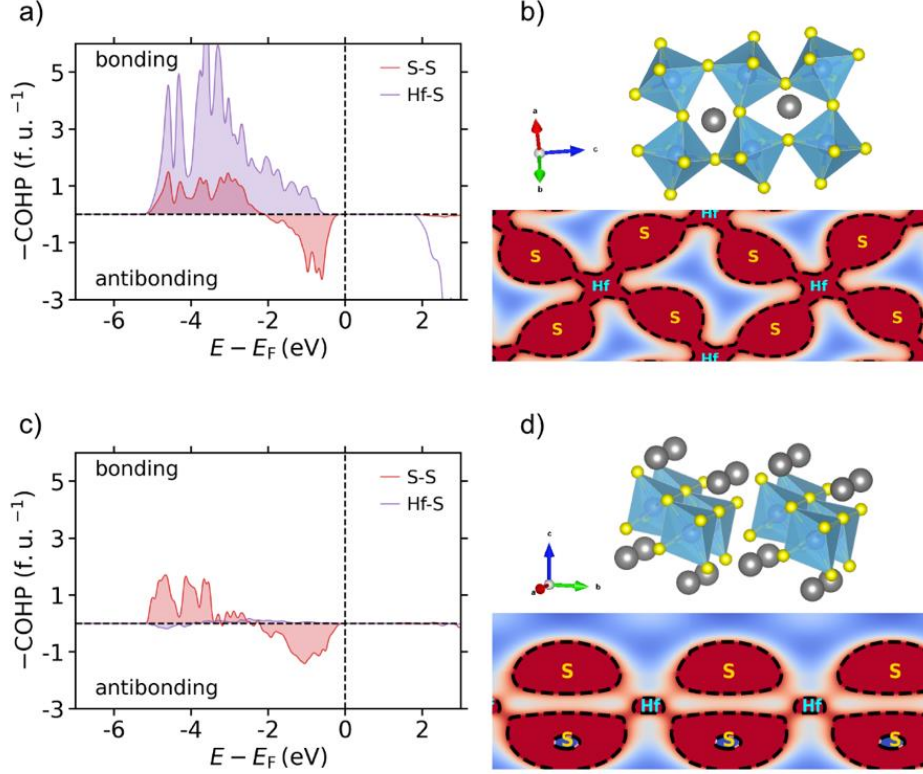


Figure 5. COHP analysis and charge density visualization for CaHfS₃ in perovskite and needle structures. (a,c) COHP curves plotted with respect to the Fermi energy (E_F) for perovskite and needle structures, respectively. Purple curves represent Hf–S interactions; red curves represent S–S interactions. COHP values are normalized per formula unit. (b,d) Two-dimensional slices of the DFT-calculated electron density as viewed along [0 0 1] and [−1 1.9 −2.5] directions for the perovskite and needle structures, respectively. Contours delineate regions of equal density. The needle phase exhibits significantly weaker *B*–*S* bonding interactions and reduced charge density between *B* and *S* sites compared to the perovskite structure.

Analysis of hull instabilities

While our COHP analysis sheds light on how covalent interactions influence polymorphic preference, ΔE_{gs} alone does not provide a complete picture of stability. **Figure 2** revisits this point, illustrating how some materials, despite being polymorphically stable, remain thermodynamically unstable due to their tendency to decompose into competing compounds in a given *A*–*B*–*S* chemical space. Much of the perovskite literature, particularly studies involving tolerance factors, tends to focus exclusively on polymorphic stability while neglecting stability with respect to competing compounds. This oversight often leads to false

positives in theoretical predictions, where materials appear stable in the perovskite structure ($\Delta E_{\text{gs}} = 0$) but are thermodynamically unstable due to highly positive decomposition energies (e.g., CaNbS_3 in **Figure 2**).

To test the validity of some of these calculations, we performed experimental synthesis reactions of materials predicted to be stable and unstable. An effective method for the synthesis of these materials is to react mixtures of binary oxides or ternary oxides with boron and sulfur.⁵⁸ The formation of low-melting and separable B_2O_3 (via solution chemistry or via vapor transport) assists in facilitating both the kinetics and thermodynamics of the reaction, as has also been shown for refractory actinide sulfides.⁵⁹ BaZrS_3 , predicted to be stable, is easily synthesized by this method (**Figure S3a**). CaTiS_3 , predicted to lie above the convex hull (+52 meV/atom), instead phase separates to CaS , Ti_3S_4 , and TiS_2 ; we also observe the formation of CaB_2O_4 (**Figure S3b**). Therefore, it is important to understand the origin of the thermodynamic instability of these compounds, particularly considering the stability of their oxide analogues (e.g., CaTiO_3 vs. CaTiS_3).

Ternary oxides are more commonly observed than their sulfide counterparts. For example, > 250 ABO_3 materials have been synthesized in the perovskite structure,³³ compared with ~25 ABS_3 perovskites (including all possible A/B sites).¹ To quantify the hull instability of ABS_3 compounds (in any structure) compared with their analogous ABO_3 compounds, we queried Materials Project³⁷ for the 81 ABO_3 oxides generated from the 81 sulfides studied in this work. Among these, 51 were available in Materials Project, of which 31 were found to lie on the convex hull. In contrast, only 15 of the 81 sulfides from our calculations are hull-stable. **Table S2** lists all available values of ΔE_{d} for this analysis. Even for those ABS_3 compounds that are thermodynamically stable (on the convex hull), their stability is marginal compared with their ABO_3 analogues. In **Figure 6**, we illustrate how the thermodynamic driving force to form ternary sulfides is generally weaker than the driving force to form the analogous oxide by showing 0 K DFT reaction energies for the formation of six ABX_3 compounds from $\text{AX} + \text{BX}_2$ reactants. In all cases, there is a larger driving force for ABO_3 compared with ABS_3 formation. One might attribute this to the inherent stability of binary sulfides, but this argument alone is insufficient, as oxides also form highly stable binary compounds, usually with higher melting points than their sulfide analogues. This suggests that additional mechanisms must be at play in stabilizing ternary oxides compared with sulfides.

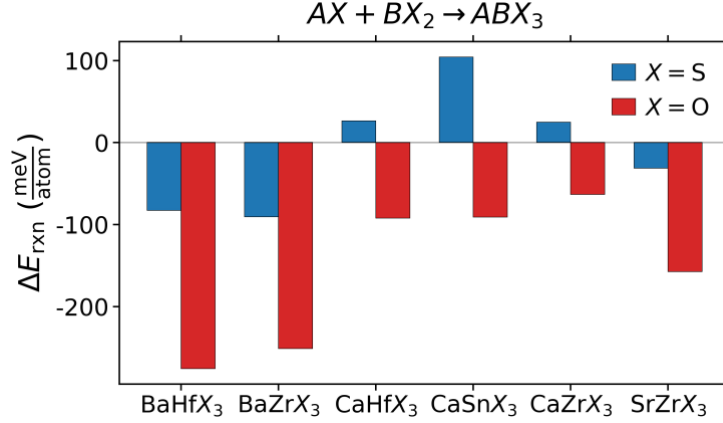


Figure 6. DFT reaction energies for $AX + BX_2 \rightarrow ABX_3$ reactions for 6 pairs of orthorhombic perovskites: BaHfX₃, BaZrX₃, SrZrX₃, CaHfX₃, CaSnX₃ and CaZrX₃ (where $X = O$ or S). The vertical position of each bar indicates its reaction energy (ΔE_{rxn}), with more negative values indicating a larger driving force to form the ABX_3 compound.

One possible mechanism is the inductive effect, which has been explored in previous studies as a potential explanation for the stabilization of ternary compounds compared with their binary counterparts. The inductive effect can be understood as an electron pressure exerted when two electropositive cations are bonded to opposite sides of an anion in an A - X - B bonding environment.⁶⁰ If A is significantly more electropositive than B , it donates additional electron density to the anion (X), which in turn strengthens the B - X bond by making it more covalent. This effect has been documented in nitride systems (among others), such as CaNiN, where the introduction of a highly electropositive Ca cation stabilizes the compound relative to its unstable Ni₃N binary.⁶¹

Ternary oxides likely benefit more from inductive stabilization than their sulfide counterparts due to the higher electronegativity of oxygen relative to sulfur. Previous studies have largely attributed the inductive effect to differences in cation electronegativity.^{60,62,63} Extending this reasoning, one can infer that the strength of the inductive effect is also influenced by the electronegativity of the anion (X). We posit that an anion with lower electronegativity will be less effective at attracting electron density from the electropositive cation, thereby diminishing the stabilizing influence of the inductive effect. To test this hypothesis, in **Table 1**, we show the change in Bader charge for the A - and B -site cations ($\Delta\delta_A$ and $\Delta\delta_B$) calculated as the difference between the cation charge in the ternary compound (ABX_3) and in its corresponding binary (AX or BX_2). We selected a subset of the compounds shown in **Figure 6** for this analysis. Separate values are presented for both sulfides and oxides. An indicator of the inductive effect is an increased charge ($\Delta\delta_A > 0$) of the A -site cation going from binary (e.g., CaO) to ternary (e.g., CaHfO₃) and a decreased charge of the B -site cation ($\Delta\delta_B < 0$) as the A - X bonds become more ionic and the B - X bonds become more covalent. Good examples to test this are CaHfX₃, CaZrX₃, and CaSnX₃. Both CaHfS₃ and CaZrS₃ have orthorhombic perovskite ground states as both oxides and sulfides, yet CaHfS₃

and CaZrS_3 exhibit slight hull instabilities ($\Delta E_d = 27$ meV/atom and 25 meV/atom, respectively), while their oxide counterparts are hull-stable. CaSnS_3 , in contrast, is both polymorphically and hull unstable in the perovskite structure ($\Delta E_{\text{gs}} = 44$ meV/atom; $\Delta E_d = 61$ meV/atom) whereas its oxide counterpart, CaSnO_3 , is a stable perovskite.

Table 1. Bader charge differences and reaction energies of selected perovskite oxides and sulfides. The Bader charge difference for the A -site ($\Delta\delta_A$) and B -site ($\Delta\delta_B$) is calculated as the charge in the ternary chalcogenide minus that in the corresponding binary compound. For example, $\Delta\delta_A = \delta(\text{Ca in CaHfS}_3) - \delta(\text{Ca in CaS})$; $\Delta\delta_B = \delta(\text{Hf in CaHfS}_3) - \delta(\text{Hf in HfS}_2)$. Also shown are the reaction energies (ΔE_{rxn} , in meV/atom) for the formation of each ternary from its binary precursors (e.g., $\text{CaS} + \text{HfS}_2 \rightarrow \text{CaHfS}_3$).

	$\Delta\delta_A$	$\Delta\delta_B$	ΔE_{rxn}
$\text{CaS} + \text{HfS}_2 \rightarrow \text{CaHfS}_3$	0.05	0.02	27
$\text{CaO} + \text{HfO}_2 \rightarrow \text{CaHfO}_3$	0.08	-0.05	-92
$\text{CaS} + \text{ZrS}_2 \rightarrow \text{CaZrS}_3$	0.05	0.02	25
$\text{CaO} + \text{ZrO}_2 \rightarrow \text{CaZrO}_3$	0.08	-0.03	-63
$\text{CaS} + \text{SnS}_2 \rightarrow \text{CaSnS}_3$	0.05	0.00	104
$\text{CaO} + \text{SnO}_2 \rightarrow \text{CaSnO}_3$	0.09	-0.05	-91

The data in **Table 1** reveals consistent trends in charge redistribution when going from binary to ternary compounds. In all systems, the A -site cation shows a larger increase in Bader charge when going from the binary to the ternary in oxides than in sulfides, indicating more electropositive behavior and stronger electron donation in oxides. Meanwhile, the B -site cation in oxides shows a clear decrease in charge from the binary to the ternary, consistent with increased covalency in the B -O bond due to the inductive effect. In contrast, sulfides show a smaller change or even an increase in B -site charge when forming the ternary. This contrasting behavior supports the notion of a weaker inductive effect in sulfides than oxides, potentially contributing to their differing thermodynamic stabilities and the relative sparsity of ABS_3 compared with ABO_3 compounds.

Conclusion

This study probes the thermodynamic stability of chalcogenide perovskites and reveals that very few are thermodynamically stable. By assessing these instabilities with respect to polymorphism and decomposition into competing compounds, we identify chemical and thermodynamic factors governing the scarcity of stable chalcogenide perovskites. In terms of polymorphism, the needle structure was calculated to be the ground-state polymorph for 77% of the 81 compounds analyzed in this study. Of the few compounds with perovskite ground-states, covalent B -S bonding was found to be a significant driver for stability. In terms of stability with respect to decomposition, we propose that a weak inductive effect for ternary sulfide formation leads to lower thermodynamic driving force for ABS_3

formation compared to analogous ABO_3 compounds. Our findings demonstrate that recently proposed tolerance factors adapted for chalcogenide perovskites tend to overpredict perovskite stability as we identify several hypothetical ABS_3 that are unstable in the perovskite structure yet lie within the bounds of these tolerance factors where perovskites are expected. While few ABS_3 perovskites are calculated to be thermodynamically stable, several hypothetical materials are computed to be weakly unstable and therefore plausibly accessible under carefully chosen synthetic conditions. In total, this work leads to new understanding of the thermodynamics and crystal chemistry of this compelling class of materials.

Acknowledgments

This work was supported by the National Science Foundation Division for Materials Research Award No. 2433203. The authors acknowledge the Minnesota Supercomputing Institute (MSI) at the University of Minnesota for providing resources that contributed to the research results reported herein. The authors also acknowledge Lauren Borgia and Yi-Ting Cheng for helpful discussions during the development of this work.

References

- (1) Sopiha, K. V.; Comparotto, C.; Márquez, J. A.; Scragg, J. J. S. Chalcogenide Perovskites: Tantalizing Prospects, Challenging Materials. *Adv. Opt. Mater.* **2022**, *10* (3), 2101704. <https://doi.org/10.1002/adom.202101704>.
- (2) Xiao, Z.; Zhou, Y.; Hosono, H.; Kamiya, T.; Padture, N. P. Bandgap Optimization of Perovskite Semiconductors for Photovoltaic Applications. *Chem. – Eur. J.* **2018**, *24* (10), 2305–2316. <https://doi.org/10.1002/chem.201705031>.
- (3) Niu, S.; Milam-Guerrero, J.; Zhou, Y.; Ye, K.; Zhao, B.; Melot, B. C.; Ravichandran, J. Thermal Stability Study of Transition Metal Perovskite Sulfides. *J. Mater. Res.* **2018**, *33* (24), 4135–4143. <https://doi.org/10.1557/jmr.2018.419>.
- (4) Gupta, T.; Ghoshal, D.; Yoshimura, A.; Basu, S.; Chow, P. K.; Lakhnot, A. S.; Pandey, J.; Warrender, J. M.; Efsthadiadis, H.; Soni, A.; Osei-Agyemang, E.; Balasubramanian, G.; Zhang, S.; Shi, S.-F.; Lu, T.-M.; Meunier, V.; Koratkar, N. An Environmentally Stable and Lead-Free Chalcogenide Perovskite. *Adv. Funct. Mater.* **2020**, *30* (23), 2001387. <https://doi.org/10.1002/adfm.202001387>.
- (5) Nishigaki, Y.; Nagai, T.; Nishiwaki, M.; Aizawa, T.; Kozawa, M.; Hanzawa, K.; Kato, Y.; Sai, H.; Hiramatsu, H.; Hosono, H.; Fujiwara, H. Extraordinary Strong Band-Edge Absorption in Distorted Chalcogenide Perovskites. *Sol. RRL* **2020**, *4* (5), 1900555. <https://doi.org/10.1002/solr.201900555>.
- (6) Wu, X.; Gao, W.; Chai, J.; Ming, C.; Chen, M.; Zeng, H.; Zhang, P.; Zhang, S.; Sun, Y.-Y. Defect Tolerance in Chalcogenide Perovskite Photovoltaic Material $BaZrS_3$. *Sci. China Mater.* **2021**, *64* (12), 2976–2986. <https://doi.org/10.1007/s40843-021-1683-0>.

- (7) Kayastha, P.; Fransson, E.; Erhart, P.; Whalley, L. Octahedral Tilt-Driven Phase Transitions in BaZrS₃ Chalcogenide Perovskite. *J. Phys. Chem. Lett.* **2025**, *16* (8), 2064–2071. <https://doi.org/10.1021/acs.jpcclett.4c03517>.
- (8) Xiao, Z.; Meng, W.; Wang, J.; Mitzi, D. B.; Yan, Y. Searching for Promising New Perovskite-Based Photovoltaic Absorbers: The Importance of Electronic Dimensionality. *Mater. Horiz.* **2017**, *4* (2), 206–216. <https://doi.org/10.1039/C6MH00519E>.
- (9) Becker, P.; Márquez, J. A.; Just, J.; Al-Ashouri, A.; Hages, C.; Hempel, H.; Jošt, M.; Albrecht, S.; Frahm, R.; Unold, T. Low Temperature Synthesis of Stable γ -CsPbI₃ Perovskite Layers for Solar Cells Obtained by High Throughput Experimentation. *Adv. Energy Mater.* **2019**, *9* (22), 1900555. <https://doi.org/10.1002/aenm.201900555>.
- (10) Xiao, Z.; Yan, Y. Progress in Theoretical Study of Metal Halide Perovskite Solar Cell Materials. *Adv. Energy Mater.* **2017**, *7* (22), 1701136. <https://doi.org/10.1002/aenm.201701136>.
- (11) Niu, S.; Zhao, H.; Zhou, Y.; Huyan, H.; Zhao, B.; Wu, J.; Cronin, S. B.; Wang, H.; Ravichandran, J. Mid-Wave and Long-Wave Infrared Linear Dichroism in a Hexagonal Perovskite Chalcogenide. *Chem. Mater.* **2018**, *30* (15), 4897–4901. <https://doi.org/10.1021/acs.chemmater.8b02279>.
- (12) Brehm, J. A.; Bennett, J. W.; Schoenberg, M. R.; Grinberg, I.; Rappe, A. M. The Structural Diversity of AB S₃ Compounds with *d* Electronic Configuration for the B - Cation. *J. Chem. Phys.* **2014**, *140* (22), 224703. <https://doi.org/10.1063/1.4879659>.
- (13) Sourisseau, C.; Cavagnat, R.; Tirado, J. L. A Raman Study of the Misfit Layer Compounds, (SnS)_{1.17}NbS₂ and (PbS)_{1.18}TiS₂. *J. Raman Spectrosc.* **1992**, *23* (11), 647–651. <https://doi.org/10.1002/jrs.1250231114>.
- (14) Okai, B.; Takahashi, K.; Saeki, M.; Yoshimoto, J. Preparation and Crystal Structures of Some Complex Sulphides at High Pressures. *Mater. Res. Bull.* **1988**, *23* (11), 1575–1584. [https://doi.org/10.1016/0025-5408\(88\)90245-0](https://doi.org/10.1016/0025-5408(88)90245-0).
- (15) Shen, X.; Cheng, D.; Zhao, H.; Yao, Y.; Liu X.; Yu R. Misfit-Layered Compound PbTiS₃ with Incommensurate Modulation: Transmission Electron Microscopy Analysis and Transport Properties. *Chin. Phys. B* **2013**, *22* (11), 116102. <https://doi.org/10.1088/1674-1056/22/11/116102>.
- (16) Saeki, M.; Onoda, M. Preparation of a Chain-Type Composite Crystal, Ba_xTiS₃ (x = 1.00 - 1.05). *J. Solid State Chem.* **1994**, *112* (1), 65–69. <https://doi.org/10.1006/jssc.1994.1265>.
- (17) Niu, S.; Huyan, H.; Liu, Y.; Yeung, M.; Ye, K.; Blankemeier, L.; Orvis, T.; Sarkar, D.; Singh, D. J.; Kapadia, R.; Ravichandran, J. Bandgap Control via Structural and Chemical Tuning of Transition Metal Perovskite Chalcogenides. *Adv. Mater.* **2017**, *29* (9), 1604733. <https://doi.org/10.1002/adma.201604733>.
- (18) Lee, C.-S.; Kleinke, K. M.; Kleinke, H. Synthesis, Structure, and Electronic and Physical Properties of the Two SrZrS₃ Modifications. *Solid State Sci.* **2005**, *7* (9), 1049–1054. <https://doi.org/10.1016/j.solidstatesciences.2005.02.010>.
- (19) Agarwal, S.; Vincent, K. C.; Agrawal, R. From Synthesis to Application: A Review of BaZrS₃ Chalcogenide Perovskites. *Nanoscale* **2025**, *17* (8), 4250–4300. <https://doi.org/10.1039/D4NR03880K>.
- (20) Hahn, H.; Mutschke, U. Untersuchungen über ternäre Chalkogenide. XI. Versuche zur Darstellung von Thioperowskiten. *Z. Für Anorg. Allg. Chem.* **1957**, *288* (5–6), 269–278. <https://doi.org/10.1002/zaac.19572880505>.

- (21) Clearfield, A. The Synthesis and Crystal Structures of Some Alkaline Earth Titanium and Zirconium Sulfides. *Acta Crystallogr.* **1963**, *16* (2), 135–142. <https://doi.org/10.1107/S0365110X6300030X>.
- (22) Yang, R.; Jess, A. D.; Fai, C.; Hages, C. J. Low-Temperature, Solution-Based Synthesis of Luminescent Chalcogenide Perovskite BaZrS₃ Nanoparticles. *J. Am. Chem. Soc.* **2022**, *144* (35), 15928–15931. <https://doi.org/10.1021/jacs.2c06168>.
- (23) Hanzawa, K.; Iimura, S.; Hiramatsu, H.; Hosono, H. Material Design of Green-Light-Emitting Semiconductors: Perovskite-Type Sulfide SrHfS₃. *J. Am. Chem. Soc.* **2019**, *141* (13), 5343–5349. <https://doi.org/10.1021/jacs.8b13622>.
- (24) Körbel, S.; L. Marques, M. A.; Botti, S. Stability and Electronic Properties of New Inorganic Perovskites from High-Throughput Ab Initio Calculations. *J. Mater. Chem. C* **2016**, *4* (15), 3157–3167. <https://doi.org/10.1039/C5TC04172D>.
- (25) Filippone, S. A.; Sun, Y.-Y.; Jaramillo, R. The Effect of an Improved Density Functional on the Thermodynamics and Adsorption-Controlled Growth Windows of Chalcogenide Perovskites. *MRS Adv.* **2018**, *3* (55), 3249–3254. <https://doi.org/10.1557/adv.2018.497>.
- (26) Kuhar, K.; Crovetto, A.; Pandey, M.; S. Thygesen, K.; Seger, B.; K. Vesborg, P. C.; Hansen, O.; Chorkendorff, I.; W. Jacobsen, K. Sulfide Perovskites for Solar Energy Conversion Applications: Computational Screening and Synthesis of the Selected Compound LaYS 3. *Energy Environ. Sci.* **2017**, *10* (12), 2579–2593. <https://doi.org/10.1039/C7EE02702H>.
- (27) Huo, Z.; Wei, S.-H.; Yin, W.-J. High-Throughput Screening of Chalcogenide Single Perovskites by First-Principles Calculations for Photovoltaics. *J. Phys. Appl. Phys.* **2018**, *51* (47), 474003. <https://doi.org/10.1088/1361-6463/aae1ee>.
- (28) Sun, Y.-Y.; Agiorgousis, M. L.; Zhang, P.; Zhang, S. Chalcogenide Perovskites for Photovoltaics. *Nano Lett.* **2015**, *15* (1), 581–585. <https://doi.org/10.1021/nl504046x>.
- (29) Perdew, J. P.; Burke, K.; Ernzerhof, M. Generalized Gradient Approximation Made Simple. *Phys. Rev. Lett.* **1996**, *77* (18), 3865–3868. <https://doi.org/10.1103/PhysRevLett.77.3865>.
- (30) Kohn, W.; Sham, L. J. Self-Consistent Equations Including Exchange and Correlation Effects. *Phys. Rev.* **1965**, *140* (4A), A1133–A1138. <https://doi.org/10.1103/PhysRev.140.A1133>.
- (31) Goldschmidt, V. M. Die Gesetze der Krystallochemie. *Naturwissenschaften* **1926**, *14* (21), 477–485. <https://doi.org/10.1007/BF01507527>.
- (32) Shannon, R. D. Revised Effective Ionic Radii and Systematic Studies of Interatomic Distances in Halides and Chalcogenides. *Acta Crystallogr. A* **1976**, *32* (5), 751–767. <https://doi.org/10.1107/S0567739476001551>.
- (33) Bartel, C. J.; Sutton, C.; Goldsmith, B. R.; Ouyang, R.; Musgrave, C. B.; Ghiringhelli, L. M.; Scheffler, M. New Tolerance Factor to Predict the Stability of Perovskite Oxides and Halides. *Sci. Adv.* **2019**, *5* (2), eaav0693. <https://doi.org/10.1126/sciadv.aav0693>.
- (34) Jess, A.; Yang, R.; Hages, C. J. On the Phase Stability of Chalcogenide Perovskites. *Chem. Mater.* **2022**, *34* (15), 6894–6901. <https://doi.org/10.1021/acs.chemmater.2c01289>.
- (35) W. Turnley, J.; Agarwal, S.; Agrawal, R. Rethinking Tolerance Factor Analysis for Chalcogenide Perovskites. *Mater. Horiz.* **2024**, *11* (19), 4802–4808. <https://doi.org/10.1039/D4MH00689E>.
- (36) Shannon, R. D. *Industrial Chemistry Library*; Academic Press Inc., 1981; Vol. 2.

- (37) Jain, A.; Ong, S. P.; Hautier, G.; Chen, W.; Richards, W. D.; Dacek, S.; Cholia, S.; Gunter, D.; Skinner, D.; Ceder, G.; Persson, K. A. Commentary: The Materials Project: A Materials Genome Approach to Accelerating Materials Innovation. *APL Mater.* **2013**, *1* (1), 011002. <https://doi.org/10.1063/1.4812323>.
- (38) Bartel, C. J. Review of Computational Approaches to Predict the Thermodynamic Stability of Inorganic Solids. *J. Mater. Sci.* **2022**, *57* (23), 10475–10498. <https://doi.org/10.1007/s10853-022-06915-4>.
- (39) Sun, W.; Dacek, S. T.; Ong, S. P.; Hautier, G.; Jain, A.; Richards, W. D.; Gamst, A. C.; Persson, K. A.; Ceder, G. The Thermodynamic Scale of Inorganic Crystalline Metastability. *Sci. Adv.* **2016**, *2* (11), e1600225. <https://doi.org/10.1126/sciadv.1600225>.
- (40) Furness, J. W.; Kaplan, A. D.; Ning, J.; Perdew, J. P.; Sun, J. Accurate and Numerically Efficient r2SCAN Meta-Generalized Gradient Approximation. *J. Phys. Chem. Lett.* **2020**, *11* (19), 8208–8215. <https://doi.org/10.1021/acs.jpclett.0c02405>.
- (41) Kresse, G.; Furthmüller, J. Efficiency of Ab-Initio Total Energy Calculations for Metals and Semiconductors Using a Plane-Wave Basis Set. *Comput. Mater. Sci.* **1996**, *6* (1), 15–50. [https://doi.org/10.1016/0927-0256\(96\)00008-0](https://doi.org/10.1016/0927-0256(96)00008-0).
- (42) Kresse, G.; Furthmüller, J. Efficient Iterative Schemes for Ab Initio Total-Energy Calculations Using a Plane-Wave Basis Set. *Phys. Rev. B* **1996**, *54* (16), 11169–11186. <https://doi.org/10.1103/PhysRevB.54.11169>.
- (43) Kresse, G.; Joubert, D. From Ultrasoft Pseudopotentials to the Projector Augmented-Wave Method. *Phys. Rev. B* **1999**, *59* (3), 1758–1775. <https://doi.org/10.1103/PhysRevB.59.1758>.
- (44) Blöchl, P. E. Projector Augmented-Wave Method. *Phys. Rev. B* **1994**, *50* (24), 17953–17979. <https://doi.org/10.1103/PhysRevB.50.17953>.
- (45) Maintz, S.; Deringer, V. L.; Tchougréeff, A. L.; Dronskowski, R. LOBSTER: A Tool to Extract Chemical Bonding from Plane-Wave Based DFT. *J. Comput. Chem.* **2016**, *37* (11), 1030–1035. <https://doi.org/10.1002/jcc.24300>.
- (46) Dronskowski, R.; Bloechl, P. E. Crystal Orbital Hamilton Populations (COHP): Energy-Resolved Visualization of Chemical Bonding in Solids Based on Density-Functional Calculations. *J. Phys. Chem.* **1993**, *97* (33), 8617–8624. <https://doi.org/10.1021/j100135a014>.
- (47) Bader, R. F. W. *Atoms in Molecules: A Quantum Theory*; International Series of Monographs on Chemistry; Oxford University Press: Oxford, New York, 1994.
- (48) Henkelman, G.; Arnaldsson, A.; Jónsson, H. A Fast and Robust Algorithm for Bader Decomposition of Charge Density. *Comput. Mater. Sci.* **2006**, *36* (3), 354–360. <https://doi.org/10.1016/j.commatsci.2005.04.010>.
- (49) Momma, K.; Izumi, F. VESTA 3 for Three-Dimensional Visualization of Crystal, Volumetric and Morphology Data. *J. Appl. Crystallogr.* **2011**, *44* (6), 1272–1276. <https://doi.org/10.1107/S0021889811038970>.
- (50) Ong, S. P.; Richards, W. D.; Jain, A.; Hautier, G.; Kocher, M.; Cholia, S.; Gunter, D.; Chevrier, V. L.; Persson, K. A.; Ceder, G. Python Materials Genomics (Pymatgen): A Robust, Open-Source Python Library for Materials Analysis. *Comput. Mater. Sci.* **2013**, *68*, 314–319. <https://doi.org/10.1016/j.commatsci.2012.10.028>.
- (51) George, J.; Petretto, G.; Naik, A.; Esters, M.; Jackson, A. J.; Nelson, R.; Dronskowski, R.; Rignanese, G.-M.; Hautier, G. Automated Bonding Analysis with Crystal Orbital Hamilton Populations. *ChemPlusChem* **2022**, *87* (11), e202200123. <https://doi.org/10.1002/cplu.202200123>.

- (52) Bystrický, R.; Tiwari, S. K.; Hutár, P.; Vančo, L.; Sýkora, M. Synthesis of Sulfide Perovskites by Sulfurization with Boron Sulfides. *Inorg. Chem.* **2022**, *61* (47), 18823–18827. <https://doi.org/10.1021/acs.inorgchem.2c03200>.
- (53) Wu, L.-M.; Seo, D.-K. New Solid–Gas Metathetical Synthesis of Binary Metal Polysulfides and Sulfides at Intermediate Temperatures: Utilization of Boron Sulfides. *J. Am. Chem. Soc.* **2004**, *126* (14), 4676–4681. <https://doi.org/10.1021/ja0392521>.
- (54) Yamaoka, S.; Okai, B. Preparations of BaSnS₃, SrSnS₃ and PbSnS₃ at High Pressure. *Mater. Res. Bull.* **1970**, *5* (10), 789–794. [https://doi.org/10.1016/0025-5408\(70\)90093-0](https://doi.org/10.1016/0025-5408(70)90093-0).
- (55) Aykol, M.; Dwaraknath, S. S.; Sun, W.; Persson, K. A. Thermodynamic Limit for Synthesis of Metastable Inorganic Materials. *Sci. Adv.* **2018**, *4* (4), eaaq0148. <https://doi.org/10.1126/sciadv.aaq0148>.
- (56) Mizoguchi, H.; Woodward, P. M.; Byeon, S.-H.; Parise, J. B. Polymorphism in NaSbO₃: Structure and Bonding in Metal Oxides. *J. Am. Chem. Soc.* **2004**, *126* (10), 3175–3184. <https://doi.org/10.1021/ja038365h>.
- (57) Young, J.; Rondinelli, J. M. Octahedral Rotation Preferences in Perovskite Iodides and Bromides. *J. Phys. Chem. Lett.* **2016**, *7* (5), 918–922. <https://doi.org/10.1021/acs.jpcclett.6b00094>.
- (58) Bystrický, R.; Tiwari, S. K.; Hutár, P.; Vančo, L.; Sýkora, M. Synthesis of Sulfide Perovskites by Sulfurization with Boron Sulfides. *Inorg. Chem.* **2022**, *61* (47), 18823–18827. <https://doi.org/10.1021/acs.inorgchem.2c03200>.
- (59) Breton, L. S.; Klepov, V. V.; zur Loye, H.-C. Facile Oxide to Chalcogenide Conversion for Actinides Using the Boron–Chalcogen Mixture Method. *J. Am. Chem. Soc.* **2020**, *142* (33), 14365–14373. <https://doi.org/10.1021/jacs.0c06483>.
- (60) Etourneau, J.; Portier, J.; Ménil, F. The Role of the Inductive Effect in Solid State Chemistry: How the Chemist Can Use It to Modify Both the Structural and the Physical Properties of the Materials. *J. Alloys Compd.* **1992**, *188*, 1–7. [https://doi.org/10.1016/0925-8388\(92\)90635-M](https://doi.org/10.1016/0925-8388(92)90635-M).
- (61) DiSalvo, F. J.; Clarke, S. J. Ternary Nitrides: A Rapidly Growing Class of New Materials. *Curr. Opin. Solid State Mater. Sci.* **1996**, *1* (2), 241–249. [https://doi.org/10.1016/S1359-0286\(96\)80091-X](https://doi.org/10.1016/S1359-0286(96)80091-X).
- (62) Kong, Y.; Song, Z.; Wang, S.; Xia, Z.; Liu, Q. The Inductive Effect in Nitridosilicates and Oxysilicates and Its Effects on 5d Energy Levels of Ce³⁺. *Inorg. Chem.* **2018**, *57* (4), 2320–2331. <https://doi.org/10.1021/acs.inorgchem.7b03253>.
- (63) Xiao, W.; Wu, D.; Zhang, L.; Zhang, X.; Hao, Z.; Pan, G.-H.; Zhang, L.; Ba, X.; Zhang, J. The Inductive Effect of Neighboring Cations in Tuning Luminescence Properties of the Solid Solution Phosphors. *Inorg. Chem.* **2017**, *56* (16), 9938–9945. <https://doi.org/10.1021/acs.inorgchem.7b01457>.

Supplementary Information

Origins of chalcogenide perovskite instability

Adelina Carr^a, Talia Glinberg^b, Nathan Stull^c, James R. Neilson^{c,d}, Christopher J. Bartel^{a*}

^a University of Minnesota, Department of Chemical Engineering and Materials Science, Minneapolis, MN 55455

^b University of Minnesota, Department of Chemistry, Minneapolis, MN 55455

^c Colorado State University, Department of Chemistry, Fort Collins, CO 80523

^d Colorado State University, School of Materials Science & Engineering, Fort Collins, CO 80523

* correspondence to cbartel@umn.edu

Table S1. DFT-calculated polymorphic stability, DFT-calculated decomposition energies, and tolerance factor predictions for ABS_3 compounds. The full dataset is provided in the accompanying file **table_S1.csv**. Radii used for the Jess tolerance factor¹ are Shannon ionic radii derived from oxides and halides²; for the Turnley tolerance factor,³ Shannon radii derived from sulfides⁴ are used. The sulfur ionic radius is 1.84 Å for the Jess factor and 1.70 Å for the Turnley factor.

Column definitions:

- **Compound:** ABS_3 compound formula
- **A / B:** *A*- and *B*-site elements
- **synthesized:** True if compound has been previously synthesized in any structure
- **calc_gs:** DFT-calculated ground state structure
- **ΔE_{gs} :** DFT-predicted energy difference between the perovskite structure and the corresponding ground-state structure
- **ΔE_d :** DFT predicted decomposition energy of the ground-state polymorph relative to the convex hull
- **tf_Jess (t^*):** Jess tolerance factor value
- **tf_Jess_pred:** predicted structure based on the Jess tolerance factor
- **rA_Jess / rB_Jess:** *A/B*-site radii used for the Jess tolerance factor
- **tf_Turnley (t^S):** sulfide-adjusted Goldschmidt tolerance factor value used in the Turnley model
- **tf_Turnley_pred:** predicted structure based on the Turnley model
- **χ_{diff} :** electronegativity difference used in the Turnley model, $\chi_{diff} = 1/5 (3\chi_S - \chi_A - \chi_B)$
- **μ :** octahedral factor value used in the Turnley model, $\mu = r_B / r_X$
- **rA_Turnley / rB_Turnley:** *A/B*-site radii used for the Turnley model
- **DOI:** reference DOI for experimentally reported compounds

Table S2. Decomposition energies relative to the convex hull for the 81 ABS_3 compounds analyzed and their 81 ABO_3 oxide analogues. The full dataset is provided in the accompanying file **table_S2.csv**. Sulfide decomposition energies are calculated in this work, while oxide decomposition energies are taken from the Materials Project database⁵ where available. Oxide entries that are not present in Materials Project are left blank.

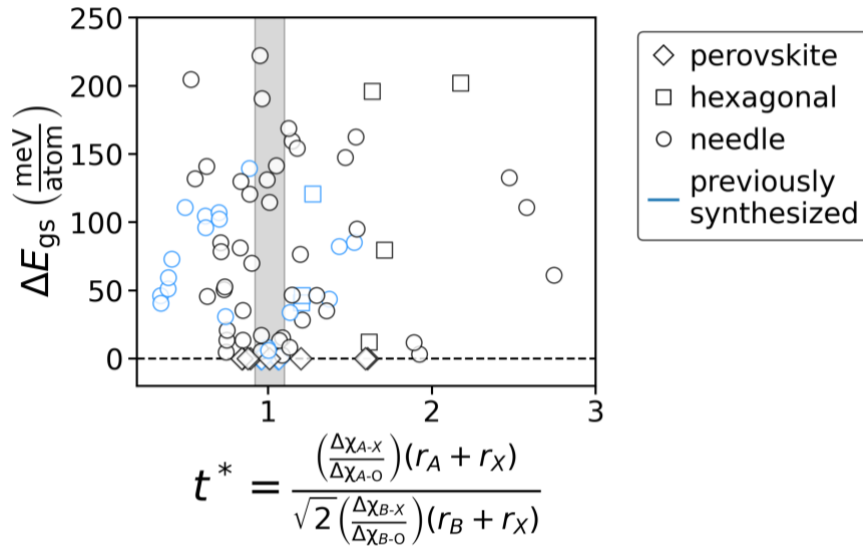


Figure S1. Expanded view of **Figure 3a**. DFT-predicted energy difference between the perovskite structure and the corresponding ground-state structure (ΔE_{gs}) plotted against the Jess tolerance factor (t^*) for all 81 materials analyzed, where points at $\Delta E_{\text{gs}} = 0$ indicate perovskite stability. The gray region denotes the t^* range where this tolerance factor predicts perovskite stability. Blue-outlined data points denote previously synthesized compounds (in any structure), and marker shapes indicate the DFT-predicted ground-state structure: diamonds for perovskite, circles for needle, and squares for hexagonal.

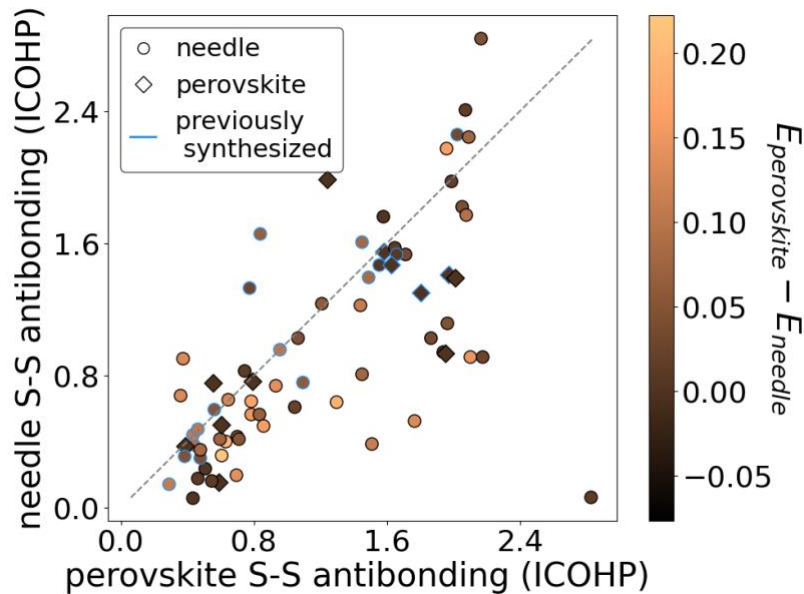


Figure S2. Parity plot comparing integrated COHP (ICOHP) values for S–S antibonding interactions in the needle and perovskite structures, normalized per formula unit and integrated from 0 to -7 eV below the Fermi level. Negative values represent bonding interactions, while positive values represent antibonding interactions. Points are colored according to the difference in energy from the perovskite

to the needle structures. Points outlined in blue correspond to previously synthesized materials. Diamond-shaped markers represent materials that have a perovskite ground state, while circles represent a needle ground state (according to our calculations). Because we compare needle and perovskite only, we have excluded materials with a hexagonal ground state. Here, we have only considered materials with differing *A*- and *B*-site atoms. The units for ICOHP are arbitrary.

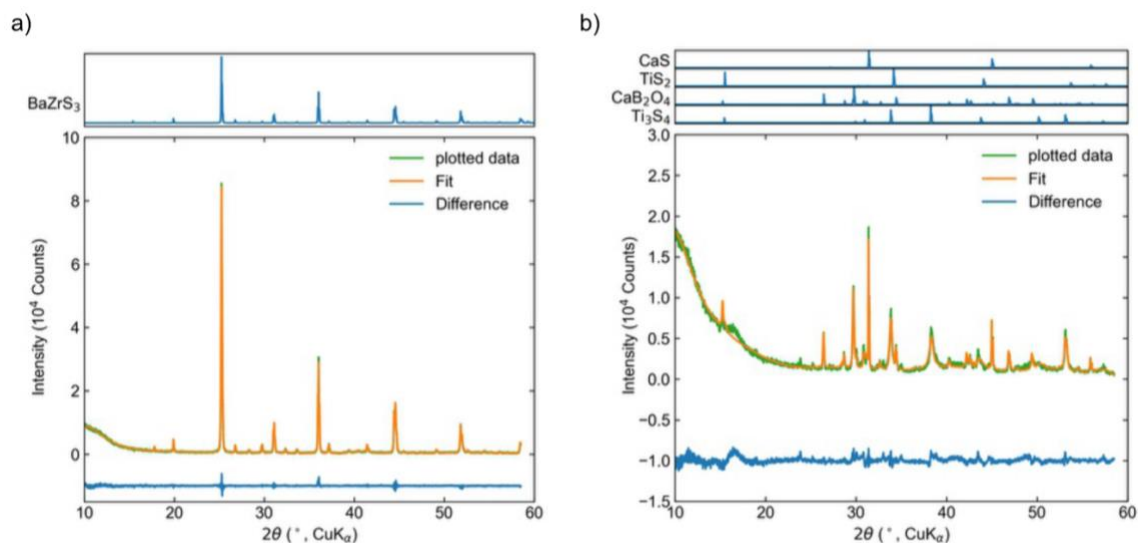


Figure S3. PXRD data for the attempted synthesis of a) BaZrS₃ and b) CaTiS₃. PXRD data showed a pure phase sample of BaZrS₃. Analysis of the PXRD data of the reaction product targeting CaTiS₃ showed multiple metal sulfide (CaS, TiS₂, and Ti₃S₄) products as well as CaB₂O₄. The reaction did not yield any Ca-Ti-S ternary phases.

- (1) Jess, A.; Yang, R.; Hages, C. J. On the Phase Stability of Chalcogenide Perovskites. *Chem. Mater.* **2022**, *34* (15), 6894–6901. <https://doi.org/10.1021/acs.chemmater.2c01289>.
- (2) Shannon, R. D. Revised Effective Ionic Radii and Systematic Studies of Interatomic Distances in Halides and Chalcogenides. *Acta Crystallogr. A* **1976**, *32* (5), 751–767. <https://doi.org/10.1107/S0567739476001551>.
- (3) W. Turnley, J.; Agarwal, S.; Agrawal, R. Rethinking Tolerance Factor Analysis for Chalcogenide Perovskites. *Mater. Horiz.* **2024**, *11* (19), 4802–4808. <https://doi.org/10.1039/D4MH00689E>.
- (4) Shannon, R. D. *Industrial Chemistry Library*; Academic Press Inc., 1981; Vol. 2.
- (5) Jain, A.; Ong, S. P.; Hautier, G.; Chen, W.; Richards, W. D.; Dacek, S.; Cholia, S.; Gunter, D.; Skinner, D.; Ceder, G.; Persson, K. A. Commentary: The Materials Project: A Materials Genome Approach to Accelerating Materials Innovation. *APL Mater.* **2013**, *1* (1), 011002. <https://doi.org/10.1063/1.4812323>.